ACS NANO

www.acsnano.org

ARTICLE

Colloidal Dispersions of Sterically and Electrostatically Stabilized PbS Quantum Dots: Structure Factors, Second Virial Coefficients, and Film-Forming Properties

Ahhyun Jeong,[○] Joshua Portner,[○] Christian P. N. Tanner, Justin C. Ondry, Chenkun Zhou, Zehan Mi, Youssef A. Tazoui, Byeongdu Lee, Vivian R. K. Wall, Naomi S. Ginsberg, and Dmitri V. Talapin*

Cite This: *ACS Nano* 2024, 18, 33864−33874

Read Online

ACCESS | Metrics & More | Article Recommendations | Supporting Information

ABSTRACT: Electrostatically stabilized nanocrystals (NCs) and, in particular, quantum dots (QDs) hold promise for forming strongly coupled superlattices due to their compact and electronically conductive surface ligands. However, studies of the colloidal dispersion and interparticle interactions of electrostatically stabilized sub-10 nm NCs have been limited, hindering the optimization of their colloidal stability and self-assembly. In this study, we employed small-angle X-ray scattering (SAXS) experiments to investigate the interparticle interactions and arrangement of PbS QDs with thiostannate ligands (PbS−$Sn_2S_6^{4-}$) in polar solvents. The study reveals significant deviations from the ideal solution behavior in electrostatically stabilized QD dispersions. Our results demonstrate that PbS−$Sn_2S_6^{4-}$ QDs exhibit long-range interactions within the solvent, in contrast to the short-range steric repulsion characteristic of PbS QDs with oleate ligands (PbS-OA). Introducing highly charged multivalent electrolytes screens electrostatic interactions between charged QDs, reducing the length scale of the repulsive interactions. Furthermore, we calculated the second virial (B_2) coefficients from SAXS data, providing insights into how surface chemistry, solvent, and size influence pair potentials. Finally, we explore the influence of long-range interparticle interactions of PbS−$Sn_2S_6^{4-}$ QDs on the morphology of films produced by drying or spin-coating colloidal solutions. The long-range repulsive term of PbS−$Sn_2S_6^{4-}$ QDs promotes the formation of amorphous films, and screening the electrostatic repulsion by the addition of an electrolyte enables the formation of crystalline domains. These findings highlight the critical role of NC−NC interactions in tailoring the properties of functional materials made of colloidal NCs.

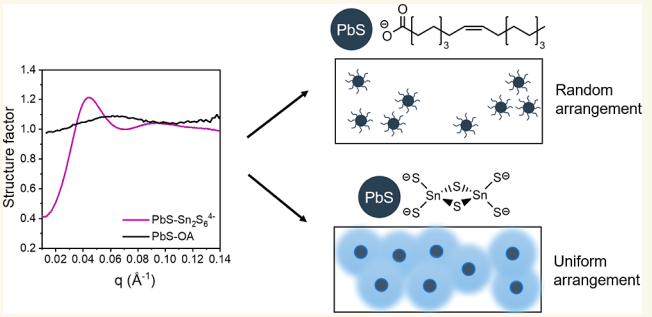

KEYWORDS: *quantum dots, SAXS, surface ligands, structure factor, second virial coefficient, self-assembly*

Colloidal nanocrystals (NCs) are crystalline nanoscale particles that are dispersed in a solvent medium. The nanocrystals of direct-gap semiconductors, also known as quantum dots (QDs), are of high technological importance.[1−4] For example, colloidal PbS QDs have been widely explored for infrared photodetectors and solar cells[5−7] and for use in field-effect transistors,[8] light-emitting diodes,[7,9] and thermoelectric devices.[8] A key advantage of QDs is the combination of physical properties inherent to inorganic semiconductors with inexpensive and scalable solution-based synthesis, processing, and device integration methods more typically associated with molecular species and polymers.

In a colloidal solution, NCs stay separated from each other by repulsive pair potentials, which prevent unwanted NC aggregation. The repulsive pair potentials can be introduced by attaching organic ligands with long flexible chains (so-called "polymer brushes") to the NC surface, thus leading to steric repulsion between NCs.[10] An alternative approach involves

Received: May 7, 2024
Revised: October 25, 2024
Accepted: October 30, 2024
Published: December 4, 2024

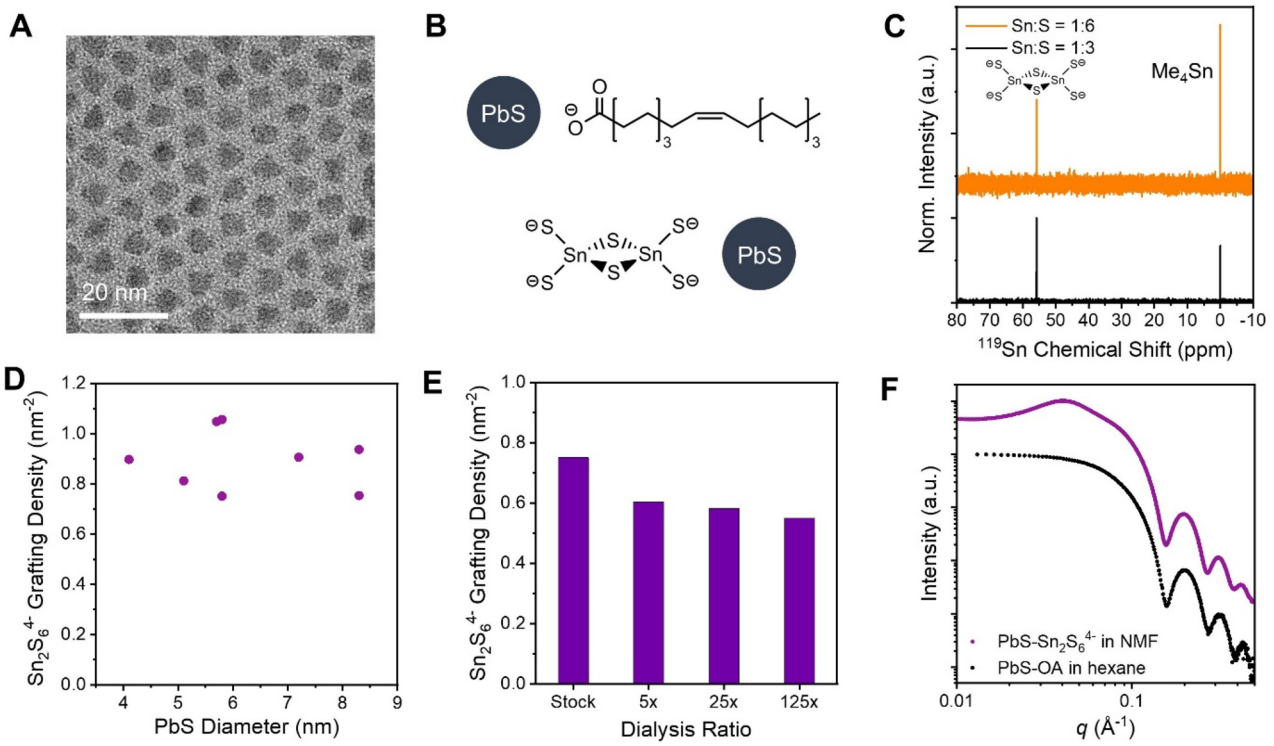

Figure 1. (A) TEM images of 5.7 nm PbS-OA QDs. (B) Chemical structures of oleate (OA) and $Sn_2S_6^{4-}$ ligands on a surface of PbS QDs. Ligands are not drawn to scale. (C) ^{119}Sn nuclear magnetic resonance (NMR) spectra of thiostannate salts synthesized in anhydrous NMF with 3:1 and 6:1 S/Sn ratios. Data are normalized to the ligand intensity, calibrated to tetramethyl tin at 0 ppm, and offset for clarity. (D) Grafting density of $Sn_2S_6^{4-}$ ligands on PbS NCs of different sizes. (E) Grafting density of $Sn_2S_6^{4-}$ ligands on 5.8 nm PbS NCs following a series of dialysis cycles. Strongly bound ligands remain in the QD concentrate, while free ligands are diluted after each cycle. (F) Log−log plot of SAXS data from 50 mg/mL 5.7 nm PbS-OA and PbS−$Sn_2S_6^{4-}$ QD solutions. Data are vertically offset for clarity.

replacing the bulky organic ligands with charged inorganic ligands such as halides (I^-, Br^-, and Cl^-) or metal chalcogenide complexes (e.g., $Sn_2S_6^{4-}$, AsS_4^{3-}, and GeS_4^{4-}), which induce repulsion between nanoparticles through the electrostatic mechanism of colloidal stabilization.[11−14] In contrast to NCs sterically stabilized with bulky organic ligands, the use of compact inorganic ligands is appealing for optoelectronic applications because they enable NCs to pack more closely, thus enhancing their electronic coupling and increasing charge carrier mobility by orders of magnitude.[15−17] This makes exciting properties possible, such as electronic minibands in the ordered arrays of strongly electronically coupled NCs,[18,19] as well as improved characteristics in optoelectronic devices. Furthermore, the short-range attractive and long-range repulsive interactions of NCs stabilized by electrostatic mechanisms can give rise to rich colloidal microphases of NCs within the solution, including the cluster fluid, percolated fluid, or periodic microphase configurations.[20] These phenomena could potentially be utilized in the bottom-up preparation of nanoscale assemblies.[21,22]

A comprehensive understanding of the NC−NC interactions in colloidal solutions is essential for making nanocrystal devices by solution processing methods or for developing bottom-up self-assembly techniques, as the interparticle interactions exert a profound impact on colloidal stability and NC assembly. Previous studies have utilized scattering and microscopy methods to experimentally study the NC−NC interactions in sterically stabilized NCs, revealing the influence of size, surface, and solvent conditions on the colloidal stability and assembly.[23−27] However, our understanding of NC−NC interactions in colloidal dispersions of electrostatically stabilized NCs remains limited. While the Derjaguin−Landau−Verwey−Overbeek (DLVO) theory offers a framework for modeling interparticle interactions of charged particles, it breaks down when the colloid is dispersed in a non-1:1 electrolyte solution or at high electrolyte concentrations.[28−31] Recent work by Coropceanu et al. has demonstrated that flocculating electrostatically stabilized NCs in a solution of high concentrations of multivalent electrolyte can induce self-assembly, which cannot be explained by the DLVO theory alone.[32−34] To develop functional materials that harness the useful properties of electrostatically stabilized NCs, a thorough understanding of how the NC size, surface chemistry, and solvent influence the interactions between electrostatically stabilized NCs will be necessary.

Here, we utilize small-angle X-ray scattering (SAXS) to study colloidal solutions of electrostatically stabilized PbS QDs. We show that sub-10 nm diameter PbS QDs colloidally stabilized with $Sn_2S_6^{4-}$ ligands (PbS−$Sn_2S_6^{4-}$) exhibit long-range interactions, resulting in complex interactions between the NCs within the solvent. In contrast, sterically stabilized PbS QDs with oleate (OA) ligands (PbS-OA) exhibit only short-range repulsions not extending beyond the full ligand length. We show that with the addition of a highly charged multivalent electrolyte, we can screen the electrostatic interactions between charged nanocrystals, resulting in short-range repulsions for electrostatically stabilized QD colloids, similar to the sterically stabilized PbS-OA QDs. Further analysis of SAXS data enabled us to determine the second virial (B_2) coefficients to quantitatively examine how surface

https://doi.org/10.1021/acsnano.4c06033
ACS Nano 2024, 18, 33864−33874

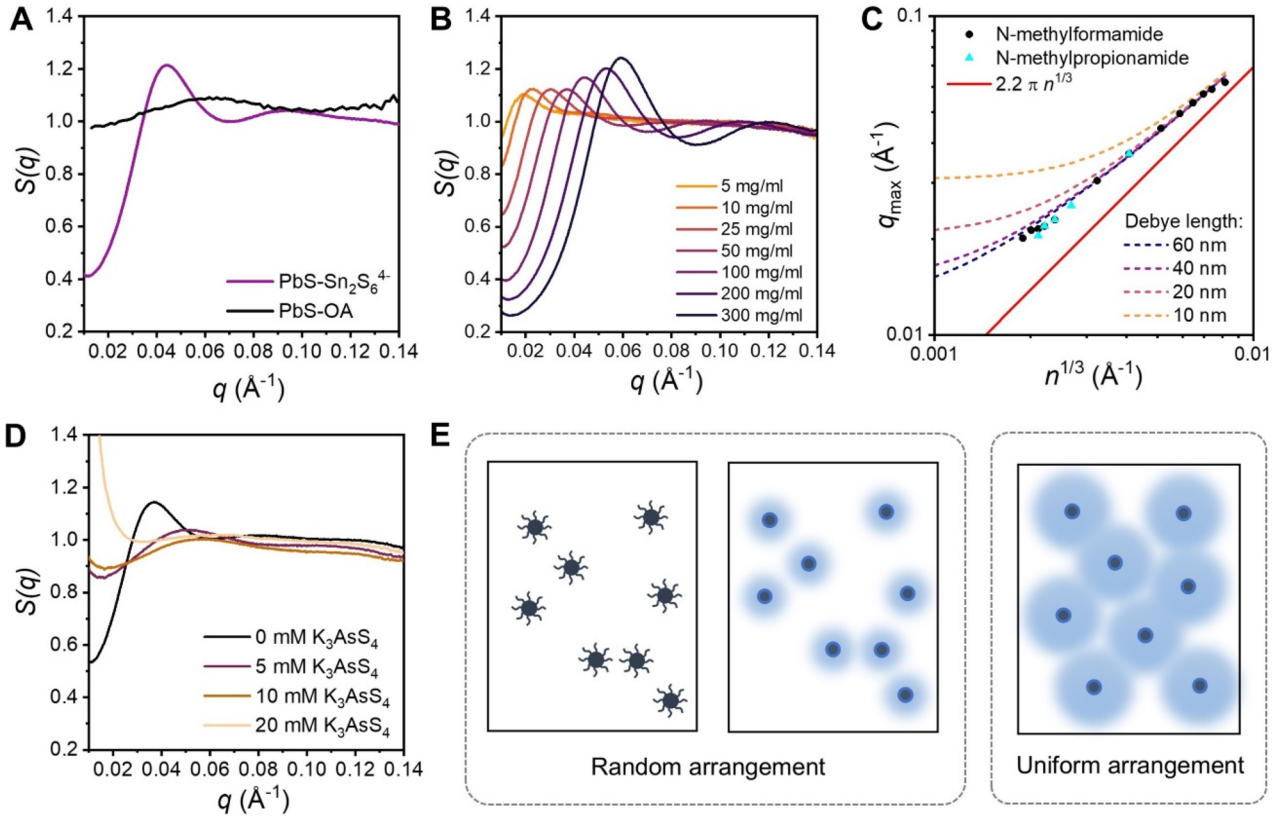

Figure 2. (A) Structure factors of colloidal dispersions of 50 mg/mL of 5.7 nm PbS QDs with different surface ligands: PbS−$Sn_2S_6^{4-}$ QDs in NMF (blue) and PbS-OA in hexane (purple). (B) Structure factors of 5.7 nm PbS−$Sn_2S_6^{4-}$ QDs in NMF at different concentrations. (C) Plot of q_{max} of 5.7 nm PbS−$Sn_2S_6^{4-}$ QDs against $n^{1/3}$ in NMF and NMPA solvents. The red line ($q_{max} = 2.2\pi n^{1/3}$) indicates the theoretical trend when NCs are separated by greatest possible distance. Dashed lines indicate the theoretical trend when NCs are separated by a Yukawa potential with a contact potential of 10 k_BT and varying Debye screening length. (D) Structure factors of 50 mg/mL of 5.7 nm PbS−$Sn_2S_6^{4-}$ QDs in NMF with different concentrations of added K_3AsS_4 salt. (E) Illustration of random arrangements of PbS-OA QDs in hexane (left), PbS−$Sn_2S_6^{4-}$ QDs in NMF with added K_3AsS_4 salts (middle), and illustration of a uniform arrangement of PbS−$Sn_2S_6^{4-}$ QDs at a low salt concentration (right).

chemistry, solvent, and composition of QDs influence their repulsive pair potentials. From these insights, we are able to identify a strategy to prepare films of strongly coupled and highly ordered superlattices of PbS QDs capped with inorganic metal chalcogenide surface ligands.

RESULTS AND DISCUSSION

Preparation and Surface Characterization of QDs. The nanocrystals used in this study include PbS QDs with diameters of 4.0 to 8.3 nm, 5.2 nm CdSe QDs, and 3.3 nm Au NCs (see Figures 1A and S1−S8). PbS QDs with precisely controlled size and narrow size distributions are synthesized from lead oleate and substituted thioureas according to the methods developed by the Owen group.[35] PbS QDs with thiostannate ligands are prepared by performing a biphasic ligand exchange on PbS-OA QDs using potassium thiostannate as a ligand source and *N*-methylformamide (NMF) as a solvent. With this ligand exchange procedure, we produced two nanocrystal populations with identical QD cores but distinct surface chemistries (Figure 1B). The PbS-OA samples are stabilized by steric repulsion between long-chain organic ligands. The thiostannate-capped PbS samples are stabilized by the electrostatic mechanism, enabled by the negatively charged surface (Table S1). Infrared spectra were taken to confirm the complete substitution of the oleic acid ligand to the thiostannate ligand (Figure S9). Thiostannate-capped CdSe QDs and Au NCs were prepared through a similar procedure.

Various thiostannate species can exist in polar solvents ($Sn_2S_6^{4-}$, $Sn_2S_7^{6-}$, and SnS_4^{4-}), so it is necessary to confirm the identity of the thiostannate ligand coordinated to PbS QDs upon ligand exchange. To verify the identity of the thiostannate species present in NMF, we conducted ^{119}Sn NMR studies. When the thiostannate salt was prepared by dissolving K_2S and SnS_2 in NMF at a 3:1 molar ratio, only one peak at 55.8 ppm was observed, corresponding to the $K_4Sn_2S_6$ species. No other species were detected in the NMR spectrum (e.g., $K_6Sn_2S_7$ at 68 ppm, K_4SnS_4 at 74 ppm).[36] Even after the addition of excess K_2S to increase the sulfur ratio, no alternative species were formed. Consequently, we concluded that $Sn_2S_6^{4-}$ is the predominant species serving as the ligand for thiostannate-capped PbS QDs in NMF, counterbalanced by the K^+ ions in the solution.

Figure 1D,E displays the grafting density of $Sn_2S_6^{4-}$ ligands on the surface of PbS QDs, determined through inductively coupled plasma optical emission spectroscopy (ICP-OES) elemental analysis assuming spherical QDs with a uniform diameter. As shown in Figure 1D, elemental analysis of PbS QDs with different sizes reveals that the grafting density of $Sn_2S_6^{4-}$ on PbS QDs before dialysis varies from 0.75 to 1.05 ligands per nm^2 and that there is no clear correlation between the size of PbS QDs and the $Sn_2S_6^{4-}$ ligand grafting density.

https://doi.org/10.1021/acsnano.4c06033
ACS Nano 2024, 18, 33864−33874

When compared to oleic acid (~2.2 ligands per nm^2),[37] the grafting density of the $Sn_2S_6^{4-}$ ligand is approximately 2−3 times smaller. To determine the concentrations of free and bound ligands, a series of dialysis experiments using centrifugal dialysis filters were conducted (Figure 1E). The dialysis filters allow the solvent and free ligands to diffuse through the membrane pores, while the larger QDs remain in the retentate. For example, the 5× dialysis cycle was performed by removing 4/5 of the solvent and free ligands using a dialysis filter followed by adding an equal volume of pure NMF to the retentate to restore the original concentration of QDs while reducing the free ligand concentration by 5 times. A dialysis ratio of 125× was achieved by repeating the 5× dialysis cycle three times. The results indicate that the grafting density of $Sn_2S_6^{4-}$ ligands on 5.8 nm PbS QDs decreases from 0.75 to 0.55 per nm^2 after 125× dialysis, suggesting that approximately 0.55 per nm^2 of $Sn_2S_6^{4-}$ ligands are strongly bound to the surface out of the initial grafting density of 0.75 per nm^2. The ligand grafting densities of PbS QDs with AsS_4^{3-} ligands and CdSe QDs are shown in the Figure S10.

Figure 1F shows representative SAXS patterns of sterically (PbS-OA) and electrostatically (PbS−$Sn_2S_6^{4-}$) stabilized PbS QDs. The scattering intensity vs momentum transfer (q) dependence in SAXS patterns of PbS-OA exhibits distinct Bessel oscillations at large $q > 0.1$ $Å^{-1}$, indicative of narrow size and shape distributions of the QDs.[38] These oscillations are preserved in the SAXS pattern of PbS−$Sn_2S_6^{4-}$ samples following the ligand exchange process. In addition, the SAXS intensity for both PbS-OA and PbS−$Sn_2S_6^{4-}$ QDs converges to a constant value at low q ($q < 0.1$ $Å^{-1}$), suggesting that both types of QDs are well-dispersed and colloidally stable in solution.[38] Unstable solutions of QDs exhibit an upturn at the low-q region, as illustrated in Figure S11. However, the low-q regions of the SAXS patterns exhibit notable differences between the two types of QDs. At small q-values (Guinier region), the scattering intensity of PbS-OA QDs converges to a horizontal line on a log−log scale, while the scattering intensity of PbS−$Sn_2S_6^{4-}$ QDs clearly deviates from a horizontal line. This indicates that colloidal dispersions of sterically and electrostatically stabilized PbS QDs have distinct structures. To examine the unusual features of the SAXS patterns of PbS−$Sn_2S_6^{4-}$ QDs in the low q region, we extracted the structure factor. The SAXS intensity is $I(q) = AP(q)S(q)$, where A is a scaling factor, $P(q)$ is the form factor, and $S(q)$ is the structure factor. The scaling factor is dependent on the measurement parameters, such as the intensity of incident X-rays and concentration and chemical composition of NCs.[38] The form factor is defined by the geometric properties of NCs, such as their size, shape, and polydispersity. $P(q)$ can be estimated by fitting the intensity in the Porod region ($qR \gg 1$), where R is NC radius, to the form factor for spherical particles (Figure S12).[38]

Structure Factors of Colloidal Solutions. The structure factor $S(q)$ is dependent on the spatial arrangement of the NCs. It provides valuable insights into the interactions between the NCs in a colloidal dispersion. If interparticle interactions are negligible, then the NCs adopt a random arrangement, resulting in a structure factor close to unity for different q-values. Conversely, when strong interparticle interactions are present, the NCs deviate from ideal gas behavior, leading to distinct features in the structure factor.[39] By analyzing $S(q)$, we can gain a better understanding of the internal structure of the NC colloid and relate it to the interparticle interactions.

Figure 2A presents a comparison of the structure factors for PbS-OA and PbS−$Sn_2S_6^{4-}$ QDs, obtained through the procedure outlined in Section 3.1 of the Supporting Information. The intensity of oscillation in the structure factor of PbS-OA QDs is observed to be smaller compared to that of PbS−$Sn_2S_6^{4-}$ QDs, indicating a more randomized distribution of particles within the colloidal solution (Figure 2E). This implies that the particles experience interparticle forces that are weak or effective over only short distances. Such behavior is expected for PbS-OA QDs, which interact only through the van der Waals (vdW) attraction and steric repulsion.[40] This behavior is in agreement with that of other sterically stabilized colloid systems.[41] On the other hand, the structure factor of electrostatically stabilized PbS QDs presents pronounced oscillatory features, indicating deviation from typical gas-like behavior. For PbS−$Sn_2S_6^{4-}$ QDs shown in Figure 2A, the structure factor shows two key characteristics: (i) $S(q)$ drops well below unity at low q, indicating that the colloids of electrostatically stabilized QDs have smaller density fluctuations over large length scales, and (ii) a peak at 0.045 $Å^{-1}$ suggests that the particles are uniformly separated by the nearest neighboring center-to-center distance (d) of ~14 nm, as calculated by $d \approx 2\pi/q_{max}$.[42] This implies that electrostatically stabilized NCs experience long-ranged repulsive forces acting on neighboring particles, resulting in the uniform arrangement illustrated in Figure 2E.[39,43]

Figure 2B demonstrates the pronounced impact of the concentration of electrostatically stabilized QDs on the structure factor. As the QD concentration rises from 1 to 300 mg/mL, the first maximum of $S(q)$ shifts from q = 0.012 $Å^{-1}$ to q = 0.060 $Å^{-1}$, signifying a reduction in the characteristic center-to-center separation between adjacent QDs from 52 to 10 nm (Figure S13). In Figure 2C, the correlation between the peak position of $S(q)$ and $n^{1/3}$ is depicted, where n is the number density of the QDs in colloidal dispersions, and $n^{-1/3}$ represents the mean center-to-center separation of particles.[44] Computational studies have shown that the peak position of the structure factor (q_{max}) of the suspension of strongly repulsive particles with Yukawa potential scales according to the relationship $q_{max} \approx 2.2\pi n^{1/3}$.[44] A strong correlation between the q_{max} of PbS−$Sn_2S_6^{4-}$ QDs in NMF and N-methylpropionamide (NMPA) and $n^{1/3}$ is observed, although the trend does not precisely align with $q_{max} = 2.2\pi n^{1/3}$ (see Figure S14 for the structure factors of PbS−$Sn_2S_6^{4-}$ QDs in NMPA). Analysis using the Yukawa potential suggests that the observed deviation originates from a small contact potential and a long Debye length.[45] The correlation between q_{max} and $n^{1/3}$ closely resembles that of 5.7 nm particles separated by the Yukawa potential, with a contact potential of 10 k_BT (Figure S15). Determining the exact Debye length of the QD colloids presents a challenge because this parameter is expected to vary significantly with the QD concentration. A simple estimation that accounts for grafting density of $Sn_2S_6^{4-}$ ligands (Figure 1E) and assuming two dissociated counterions (K^+) per surface-bound $Sn_2S_6^{4-}$ unit suggests that the Debye length can approach ~40 nm in dilute (1 mg/mL) solutions of PbS QDs, which drops to just a few nanometers when the concentration of PbS QDs increases to 100 mg/mL and higher (Table S2). In highly concentrated QD solutions, we expect significant deviations from DLVO due to ion−ion correlations.

https://doi.org/10.1021/acsnano.4c06033
ACS Nano 2024, 18, 33864−33874

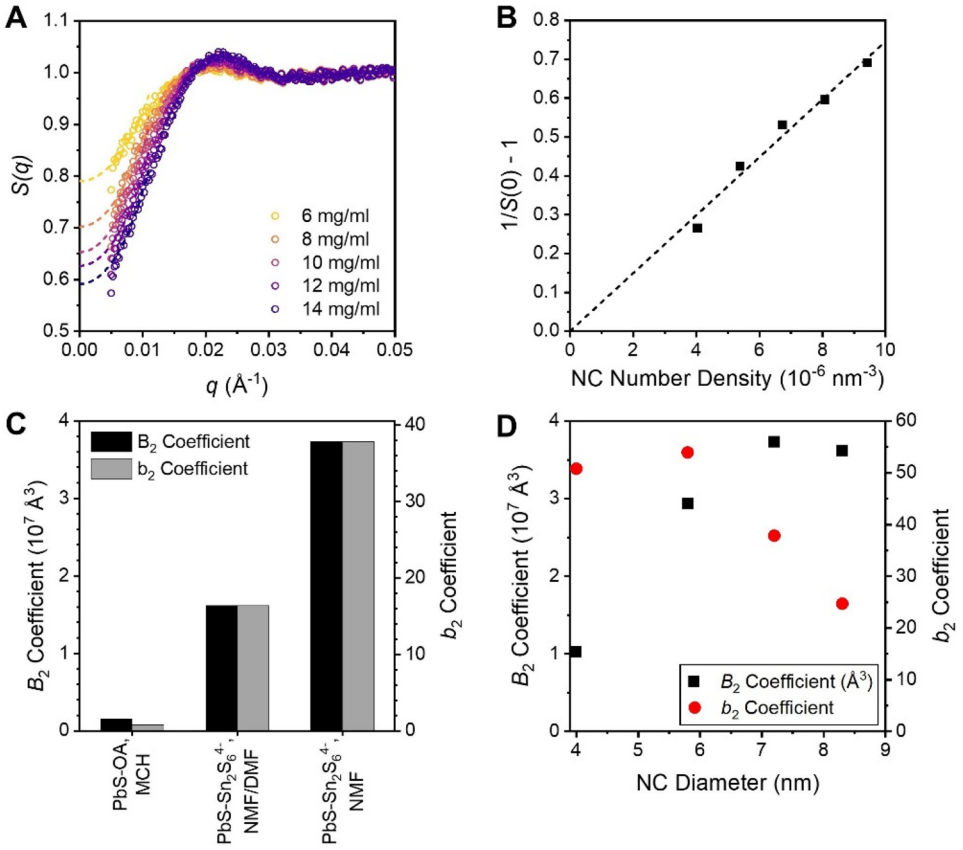

Figure 3. (A) Structure factor $[S(q)]$ of 7.2 nm PbS QDs with $Sn_2S_6^{4-}$ ligands in NMF. The dashed lines are fits of $S(q)$ to $S(q) = A\exp(kq^2)$ in the low-q region. The circles are experimentally determined $S(q)$ values. (B) Corresponding plot of $1/S(0)$-1 against the number density of PbS QDs. (C) B_2 and b_2 coefficients of ~7 nm PbS QDs with different surface chemistries and solvent conditions. The diameters of PbS-OA and PbS−$Sn_2S_6^{4-}$ NCs are 6.9 and 7.2 nm, respectively. NMF/DMF indicates a mixture of NMF and DMF in a 7:3 volume ratio. (D) B_2 and b_2 coefficients of PbS−$Sn_2S_6^{4-}$ QDs in NMF with QD diameters ranging from 4.0 to 8.3 nm.

In Figure 2B, we also observe that the peak-to-valley ratio of the structure factor increases with the increasing concentration. The ratio of the value of structure factor at $q = 0$, i.e., $S(0)$ and the peak value of the structure factor (S_{max}) is known as the hyperuniformity index, which quantifies the spatial uniformity of the arrangement of particles.[46] At low concentrations, interparticle repulsions are weak due to an exponential decay of electrostatic repulsion with distance. This allows the QDs to adopt a random arrangement, reflected by the near-unity value of $S(0)/S_{max}$. On the other hand, in a concentrated solution of PbS QDs, strong electrostatic repulsions force the NCs to be separated by relatively uniform distances, as evidenced by the intense primary peak and the depression of $S(q)$ at small q values (Figure S16). Despite this uniform arrangement, the QDs remain far from a "jammed" structure, where the QD movement is restricted by repulsive forces from neighboring particles. X-ray photon correlation spectroscopy measurements confirm that the diffusion rates of QDs in dilute and concentrated solutions of PbS−$Sn_2S_6^{4-}$ QDs show negligible differences (Figure S17).[47] This is likely due to the insufficient strength of interparticle repulsion of the QDs to confine the movement of the QDs at these volume fractions. Potential applications of uniformly arranged particles with no translational order include optically isotropic waveguides and sources of isotropic thermal radiation.[46,48]

The addition of free ions to an electrostatically stabilized PbS−$Sn_2S_6^{4-}$ QD solution is expected to reduce the screening length of electrostatic repulsion.[49] Consequently, the long-range repulsion of NCs is reduced, resulting in the reappearance of a colloidal gas-like configuration (Figure 2E). This phenomenon is corroborated by the structure factors shown in Figure 2D, where the oscillatory features of the structure factor are suppressed by the addition of K_3AsS_4 salt. The addition of 10 mM K_3AsS_4 results in near-unity $S(q)$, similar to the case of sterically stabilized PbS-OA QDs. Notably, the rise of structure factors in the low-q region may be attributed to transient aggregation of PbS QDs that yield strong X-ray scattering in this range, due to the competing effects of short-range attraction, which promotes clustering of the QDs, and the long-range repulsion that prevents the growth of the aggregates into macroscopic size.[42,50]

Second Virial Coefficients. To quantitatively analyze how the size, surface, and solvent of NCs impact the extent of deviation from ideal behavior, we measured the second virial (B_2) coefficients of colloidal dispersions of electrostatically stabilized PbS QDs. Various physical properties of nonideal solutions can be defined through virial coefficients. Thus, the osmotic pressure (Π) of a dispersion of interacting particles can be expressed as a power series of particle number density (n), where k_B is the Boltzmann constant, T is the temperature, B_2 is the second virial coefficient, and B_3 is the third virial coefficient[51]

$$\frac{\Pi}{k_B T} = n + B_2 n^2 + B_3 n^3 + \cdots \quad (1)$$

https://doi.org/10.1021/acsnano.4c06033
ACS Nano 2024, 18, 33864−33874

A positive or negative B_2 coefficient indicates a net repulsive or net attractive pairwise interaction between the particles, respectively. Quantitatively, B_2 can be directly related to the pair potential $u(r)$ between NCs that are separated by the distance r[41]

$$B_2 = -2\pi \int_0^\infty \left(\exp\left(-\frac{u(r)}{k_B T} \right) - 1 \right) r^2 \, dr \quad (2)$$

When comparing the B_2 coefficients of different NC samples, it is often convenient to calculate the normalized second virial coefficients (b_2), which provide more direct insights into colloidal stability and self-assembly behavior. For spherical or nearly spherical particles, dimensionless b_2 can be calculated as $b_2 = B_2/B_{2,HS}$, where $B_{2,HS}$ is the second virial coefficient of an equivalent colloid of hard spheres. In turn, $B_{2,HS}$ can be calculated as $B_{2,HS} = 2\pi (d + 2\delta)^3/3$, where d is the diameter of the NC core and δ is the length of the surface ligands.[41] A positive b_2 value implies an overall repulsive interaction between NCs, leading to high colloidal stability. In contrast, a negative b_2, especially $b_2 < -10$, typically leads to uncontrolled aggregation into an amorphous structure.[52] Weakly attractive particles with a small b_2 coefficient ($-10 < b_2 < -1$) can self-assemble into ordered structures, such as protein crystals or NC superlattices.[32−34,52]

In this section, we experimentally determine the B_2 coefficients for PbS QDs from concentration-dependent SAXS data. Then, we compare our results with predictions from DLVO theory, which provides a minimalistic framework to describe the interparticle interactions of charged colloidal particles.[29−31] The relationship between the number density (n) of NCs and the B_2 coefficient is described by eq 3, where $S(0)$ is the extrapolated value of structure factor at $q = 0$ and $O(n^2)$ collects the higher-order terms in n[41]

$$\frac{1}{S(0)} = 1 + 2B_2 n + O(n^2) \quad (3)$$

The value of $S(0)$ can be obtained by performing a linear fit of $\ln [S(0)]$ against q^2 at small q values (Figure S18).[53] Figure 3A displays representative plots of $S(q)$ and the corresponding fits for $S(0)$ in the low-q regions for a series of concentrations of 7.2 nm PbS QDs with $Sn_2S_6^{4-}$ ligands in NMF. The dashed lines are fits obtained by the procedure outlined in the Section 4.1 of the Supporting Information. Figure 3B shows a representative plot of $1/S(0)$-1 against the NC number density (n), allowing the B_2 coefficient to be determined from the slope. The structure factor and B_2 analyses for all other QDs are shown in Figure S19. To minimize possible effects of PbS−$Sn_2S_6^{4-}$ QD concentration on the Debye length, and correspondingly on the B_2 coefficient, the B_2 coefficients of different QD samples have been measured in an identical concentration regime (6−14 mg/mL).

Figure 3C presents the B_2 and b_2 coefficients of ∼7 nm PbS-OA and PbS−$Sn_2S_6^{4-}$ QDs. Notably, all QDs exhibit positive b_2 coefficients, indicating the presence of repulsive interactions among the particles. The 7.2 nm PbS QDs that are electrostatically stabilized by $Sn_2S_6^{4-}$ ligands ($b_2 > 16$) demonstrate significantly larger b_2 coefficients compared to the sterically stabilized 6.9 nm PbS-OA NCs ($b_2 = 0.76$) in methylcyclohexane (MCH). This observation is consistent with the finding that the electrostatically stabilized QDs deviate far more from ideal gas behavior compared to sterically stabilized NCs due to their long-range interactions. The large b_2 coefficients of 5.2 nm CdSe−$Sn_2S_6^{4-}$ QDs ($b_2 = 68.2$) and 3.3 nm Au−$Sn_2S_6^{4-}$ NCs ($b_2 = 63.2$) in NMF further illustrate that the electrostatically stabilized NCs with thiostannate ligands generally exhibit strong interparticle repulsions regardless of NC material. The pair potential of these NCs predicted through the DLVO model can be found in Figure S20.

The b_2 coefficients of PbS−$Sn_2S_6^{4-}$ NCs were measured in NMF and a mixture of NMF and *N*,*N*-dimethylformamide (DMF) in a 7:3 volume ratio (Figure 3C). The b_2 coefficient of 7.2 nm PbS−$Sn_2S_6^{4-}$ NCs in the NMF/DMF mixture ($b_2 = 16.4$) is significantly lower than that in NMF ($b_2 = 37.8$). This is because the dielectric constant of NMF ($\varepsilon_{NMF} \sim 170$) is much larger than that of the NMF/DMF mixture ($\varepsilon_{NMF/DMF} \sim 130$),[54,55] resulting in stronger ion−dipole interactions between the surface ligands of the PbS−$Sn_2S_6^{4-}$ NCs and the solvent molecules (Figure S21), as described by the DLVO theory. These interactions contribute to the enhanced colloidal stability of the NCs in solvents with a high dielectric constant.

In Figure 3D, we present the B_2 and b_2 coefficients of four different PbS−$Sn_2S_6^{4-}$ QDs in NMF, ranging in size from 4.0 to 8.3 nm. Notably, the B_2 coefficient generally increases with the QD diameter. This can be attributed to the increased surface area of the QDs that exhibit repulsive forces, as well as the increased volume of space that each QD occupies. This trend is consistent with the predictions from the DLVO theory (Figure S22). Conversely, the b_2 coefficient generally decreases with the increasing QD diameter, which is also consistent with the DLVO theory. In general, independence of b_2 and QD diameter suggests that the interparticle interaction range scales with the QD size, implying a Debye length that scales linearly with QD radius (R). A decreasing b_2 trend, though, indicates that the Debye length either grows more slowly than linearly in the QD diameter, remains independent of QD diameter, or even decreases with an increasing QD diameter. If no additional electrolyte is added and ligand grafting density is independent of QD size as found in Figure 1D, the Debye length, κ^{-1}, defined by the concentration of counterions required for charge neutrality, should scale as $\kappa^{-1} \propto \sqrt{R}$. If the ionic concentration in solution is set by added electrolyte, κ^{-1} should be independent of the QD diameter. Both of these limiting cases result in decreasing b_2 with increasing QD size, in agreement with the experimental data.

Our results indicate that the size- and solvent-dependent trends of the B_2 coefficients generally align with DLVO theory predictions, suggesting that DLVO theory is a powerful tool for modeling the behavior of electrostatically stabilized nanoparticles. However, we also found that DLVO calculations tend to underestimate the B_2 coefficients, highlighting that the theory does not fully capture the interparticle interactions of colloidal QDs (Table S3). This discrepancy can be attributed to the following two assumptions of DLVO theory that do not align with our system. First, the DLVO theory is reasonably accurate for dilute 1:1 electrolytes, but concentrated and especially multivalent electrolytes show ion−ion correlations not accounted for by the DLVO theory. Second, DLVO theory relies on the Derjaguin approximation, which approximates curved surfaces as a series of parallel walls. This is a reasonable approximation in a colloid of micrometer-sized particles, where the radius of the curvature is large. However, due to the nanoscale size of the nanocrystals, the curvature of the particles is non-negligible, and hence, the Derjaguin approximation is likely to fail.

https://doi.org/10.1021/acsnano.4c06033
ACS Nano 2024, 18, 33864−33874

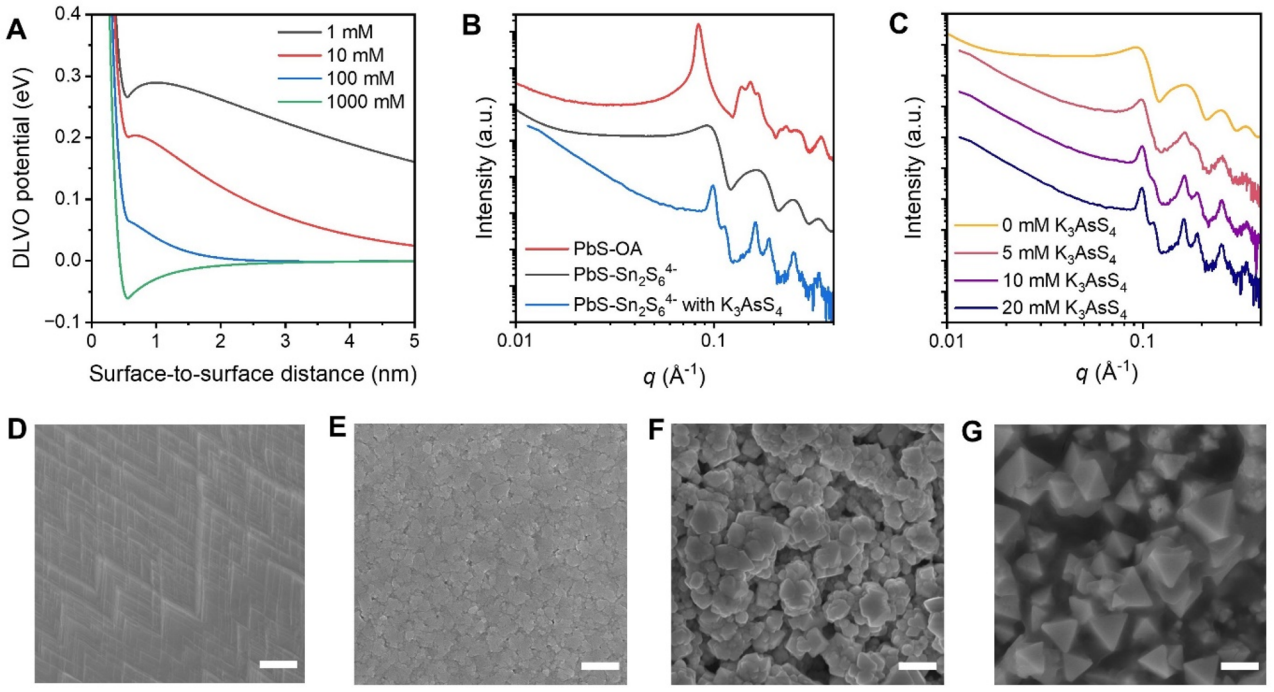

Figure 4. (A) DLVO potentials for 7.2 nm PbS−$Sn_2S_6^{4-}$ QDs in NMF with varying concentrations of added multivalent electrolyte, e.g., K_3AsS_4 salt. (B) SAXS patterns of films of 7.2 nm PbS QDs with different ligands drop-cast on a thin Si wafer. (C) SAXS patterns of PbS−$Sn_2S_6^{4-}$ QD films drop-cast on a thin Si wafer, with varying concentration of K_3AsS_4 added. (D−G) Scanning electron microscopy (SEM) images of films of (D) PbS-OA QDs, (E) PbS−$Sn_2S_6^{4-}$ QDs, and (F) PbS−$Sn_2S_6^{4-}$ QDs with added 20 mM K_3AsS_4 and (G) PbS−$Sn_2S_6^{4-}$ QDs with 86 mM K_3AsS_4 added. All films were prepared by drop-casting. Scale bars in SEM images are 1 μm.

Films Formed from Colloids of Sterically and Electrostatically Stabilized NCs. In the previous sections, we showed that colloidal dispersions of electrostatically stabilized nanocrystals exhibit long-range repulsive forces. Within the framework of DLVO theory, the range of the repulsive forces is defined by the Debye screening length, and addition of an electrolyte into colloidal dispersion increases ionic strength and reduces the Debye length.[28] According to several theoretical and computational studies,[56−61] the long-ranged electrostatic interactions between NCs should impact rheological properties and many other characteristics of colloidal dispersions.

The exact form of pair potentials for colloidal sub-10 nm NCs cannot be easily extracted from available experimental data.[62] It is generally accepted, though, that pair potentials between electrostatically stabilized NCs should include at least three components: electrostatic repulsion, vdW attraction, and a steep short-range repulsion at hard contact of NC cores. Although exact parameters of NC pair potentials may be difficult to access, it has been demonstrated that the behavior of PbS−$Sn_2S_6^{4-}$ NCs at high ionic strengths resembles the behavior of spheres with a pair potential consisting of a narrow attractive well with the width less than 20% of NC diameter and depth of several k_BT.[32−34] At low ionic strengths, the interparticle interactions can be modeled as a combination of short-range attractive and longer-range repulsive potentials, with the possibility of changing the contributions of attractive and repulsive components by varying the concentration of free ions added to a colloidal dispersion (Figure 4A). In contrast, sterically stabilized NCs in nonpolar solvents behave very nearly as hard spheres.[41] Only when the solvent evaporates do the hydrocarbon chains of ligands begin experiencing strong vdW attractions.[63]

Given the importance of colloidal QDs for thin-film optoelectronic devices, we aim to compare the films of PbS QDs prepared from colloidal solutions of sterically and electrostatically stabilized colloidal dispersions and evaluate what characteristics of the pair potentials are most favorable for the formation of dense and uniform layers desirable for LEDs, photodetectors, solar cells, and other thin-film devices. The structure and morphology of these films prepared under different conditions, as characterized by SAXS and SEM, are shown in Figure 4B−G.

Drop-casting or spin-coating of colloidal solutions of sterically stabilized PbS-OA QDs typically results in ordered films containing multiple superlattice domains. The domain size is defined by the solvent evaporation rate and is smaller for spin-coated films compared to that in films made by slow solvent evaporation (Figure 4D and S23). Interestingly, the phase of superlattices can be either face-centered cubic (*fcc*) or body-centered cubic (*bcc*). For example, our films of 7.2 nm PbS-OA QDs deposited from methylcyclohexane have an *fcc* structure (Figures 4B, S24 and S25). In several theoretical studies which related pair potentials and phase diagrams of colloidal spheres, it has been shown that the *fcc* phase is more favorable for particles that interact by hard sphere-like potentials, due to the higher packing density. Thus, very similar 7 nm PbS-OA QDs in toluene formed *fcc* superlattices upon slow addition of ethanol, which increased solvent polarity and gradually changed repulsive pair potentials to become attractive.[64]

In contrast, electrostatically stabilized PbS−$Sn_2S_6^{4-}$ QDs show a more complex behavior. In the absence of added ions, spin-coated or drop-cast colloidal dispersions of PbS−$Sn_2S_6^{4-}$ QDs in NMF yield glassy films with no QD ordering (Figure 4B and S24).[65] The formation of disordered films is consistent

https://doi.org/10.1021/acsnano.4c06033
ACS Nano 2024, 18, 33864−33874

with theoretical predictions for particles interacting through short-range attractive and long-range repulsive potentials.[56] In such systems, when the NC concentration increases due to solvent evaporation, the narrow attractive well promotes the formation of NC clusters which cannot grow further into superlattices due to the repulsive term.[57,59] Upon further increase of NC concentration, these clusters coalesce, forming percolated networks of NCs and even microphases.[20] Computational studies also predict that NC colloids with short-range attraction and long-range repulsive potentials are prone to gelation, also leading to disordered NC layers.[59] The randomly packed glassy NC layers are expected to have more isotropic properties compared with crystalline superlattices (Figure 4E and S23), which could be useful for applications in optoelectronic devices.

The addition of free ions, e.g., by adding K_3AsS_4 salt to the colloidal dispersion, whose concentration is gradually increasing upon solvent evaporation, is expected to suppress both the amplitude and the range of repulsive component, as shown in Figure 4A. As shown in our previous study, a strong decrease of the repulsive term is favorable for self-assembly of NCs into long-range ordered *fcc* superlattices[32] because nucleated clusters of NCs can keep growing indefinitely. Figure 4C and S24 show that the addition of K_3AsS_4 salt to 7.2 nm PbS−$Sn_2S_6^{4-}$ QDs increases the ordering of QDs in both drop-casted and spin-coated films. Ultimately, the film becomes a layer of faceted superlattices of PbS QDs, as shown in Figure 4F,G. Individual superlattices have nearly perfect octahedral faceting, corresponding to the Wulff construction with low energy facets with $(111)_{SL}$ Miller indices. The formation of such structures is expected if NCs have a strong tendency to self-assemble into crystalline superlattices, while maximization of total cohesive energy through densification of the NC layer is not happening. In one plausible scenario, superlattices of PbS−$Sn_2S_6^{4-}$ QDs nucleate and grow at the early stage of film drying, and the precipitation of micron-size superlattices results in a pile of faceted superlattices (Figure 4G and S23). Naturally, the long-range electronic connectivity for such film morphology is relatively weak, and, despite the possibility for interesting physics (e.g., miniband formation) within superlattices of strongly electronically coupled QDs,[18] the utility for such layers for optoelectronic applications is questionable.

Varying the concentration and nature of free ions in solution allows for tuning of the pair potentials from long-range strongly repulsive, resulting in amorphous NC films, to short-range attractive that yields perfect but loosely packed QD superlattices. In between these limiting cases, there exists a "sweet spot" where QDs self-assemble into ordered domains that are shaped to connect with neighboring QD superlattices without gaps. Such a morphology maximizes packing density and electronic coupling both within and between superlattice domains and enables good electronic connectivity across the entire NC film. Indeed, using a small concentration of free ions (no added K_3AsS_4 salt, but also no excessive washing of 7.2 nm PbS−$Sn_2S_6^{4-}$ QDs, which removes trace residual electrolyte) allowed us to achieve the morphology shown in Figure S26. It demonstrates that electrostatically stabilized colloidal dispersions of semiconductor QDs can be used as "inks" for making QD layers with packing density and structural quality comparable to those in films prepared from colloids of sterically stabilized NCs.

CONCLUSIONS

In this study, we compare the interparticle interactions of sterically and electrostatically stabilized PbS QDs using SAXS measurements and the influence of solvent and ionic composition on the structure and film-forming properties of PbS QDs. This comprehensive study of the structural factors has revealed that electrostatically stabilized QDs exhibit strong QD−QD interactions that persist over long distances, a characteristic absent from conventionally sterically stabilized QDs. However, the introduction of salts like K_3AsS_4 can reduce this interaction range, restoring short-range interactions similar to those seen in sterically stabilized QDs. Further analysis of the structure factors of electrostatically stabilized colloidal dispersions of PbS QDs with different sizes (4.0−8.3 nm) and surface chemistries ($Sn_2S_6^{4-}$, AsS_4^{3-}) and in different polar solvents (NMF, NMPA, and DMF) revealed that the solutions of electrostatically stabilized QDs exhibit significant deviation from ideal solution behavior. The correlations between the experimental B_2 coefficients and various experimental factors were found to be qualitatively consistent with the predictions of the DLVO model, although the experimental B_2 coefficients were consistently larger than the values predicted from the DLVO model. This may be attributed to the complex interactions of counterions (K^+) and multivalent ions ($Sn_2S_6^{4-}$), which cannot be fully captured by the DLVO model.

Our results provide insight into the influence of interparticle interactions in the morphology of thin films. Weakly repulsive particles, such as sterically stabilized PbS-OA QDs, tend to form crystalline or polycrystalline films, while strongly repulsive particles such as electrostatically stabilized PbS−$Sn_2S_6^{4-}$ QDs tend to form amorphous films. The addition of the K_3AsS_4 salt reduces the interactions and enables crystalline film formation for PbS−$Sn_2S_6^{4-}$ QDs. These findings underscore the importance of QD−QD interactions in tailored film deposition and functional nanomaterials.

METHODS/EXPERIMENTAL SECTION

Synthesis of PbS-OA QDs. The synthesis of PbS-OA QDs follows a previously reported method.[35] After washing, the samples were stored under a N_2 atmosphere in anhydrous methylcyclohexane (MCH) or anhydrous *n*-hexane.

Ligand Exchange. The ligand exchange of PbS-OA into PbS−$Sn_2S_6^{4-}$ QDs was adapted from a previously reported procedure.[32]

SAXS Measurements. Most SAXS data in Figures 1−4 of the main text were collected at beamline 12-ID-B, Advanced Photon Source in Argonne National Laboratory. The beam energy was 12.7 keV, and the beam size was ∼0.5 mm. Colloidal QDs were measured in glass capillaries that were flame-sealed in air. Films of QDs were prepared and measured on a 50−75 μm thick Si wafer. A few SAXS data sets in Figure 1F (SAXS intensity of PbS-OA), Figure 2A (structure factor of PbS-OA), and Figure 4B (SAXS intensity of PbS−$Sn_2S_6^{4-}$ with the K_3AsS_4 film) were instead collected using a SAXSLAB Ganesha Instrument with a Cu K-alpha source. Colloidal QD solutions were contained in glass capillaries that were flame-sealed in air. Films of QDs were prepared and measured on boron-doped 50−75 μm thick Si wafers.

Film Preparation. For SEM measurements, a 525 μm thick nitrogen-doped Si wafer with a 300 nm layer of dry-grown thermal oxide was cleaned by sonicating successively in hexane, acetone, DI water, and isopropanol for 5 min each. To prepare the films for PbS-OA QDs, the surface of the wafer was treated by spin-coating it with hexamethyldisilazane (HMDS) at 3000 rpm for 45 s, followed by annealing it at 150 °C for 30 min. A solution of PbS-OA in MCH was drop-cast onto the wafer, and the solvent was allowed to evaporate

https://doi.org/10.1021/acsnano.4c06033
ACS Nano 2024, 18, 33864−33874

under ambient pressure and temperature. During evaporation, the wafer was tilted by ∼10° by placing one edge on a glass microscope slide. To prepare the films for PbS−$Sn_2S_6^{4-}$ QDs, the same cleaning method was used, but instead of HMDS treatment, the surface of the wafer was treated with oxygen plasma (Harrick Plasma, Plasma Cleaner PDC-001) for 15 min before transferring to a dry N_2 glovebox. A solution of PbS−$Sn_2S_6^{4-}$ in NMF was drop-cast onto the wafer, and the solvent was allowed to evaporate under vacuum. The wafer was similarly tilted by ∼10° during the evaporation process.

For SAXS measurements, solutions of QDs were drop-cast onto a boron-doped Si wafer with a thickness of 50−75 μm. MCH was allowed to evaporate under ambient temperature and pressure, and NMF was allowed to evaporate under a vacuum.

ASSOCIATED CONTENT

Supporting Information

The Supporting Information is available free of charge at https://pubs.acs.org/doi/10.1021/acsnano.4c06033.

Detailed descriptions of the experimental methods, nanocrystal and nanocrystal film characterization, SAXS analysis, and DLVO theory analysis (PDF)

AUTHOR INFORMATION

Corresponding Author

Dmitri V. Talapin − *Department of Chemistry, James Franck Institute, and Pritzker School of Molecular Engineering, University of Chicago, Chicago, Illinois 60637, United States; Center for Nanoscale Materials, Argonne National Laboratory, Argonne, Illinois 60439, United States;* orcid.org/0000-0002-6414-8587; Email: dvtalapin@uchicago.edu

Authors

Ahhyun Jeong − *Department of Chemistry, James Franck Institute, and Pritzker School of Molecular Engineering, University of Chicago, Chicago, Illinois 60637, United States*

Joshua Portner − *Department of Chemistry, James Franck Institute, and Pritzker School of Molecular Engineering, University of Chicago, Chicago, Illinois 60637, United States*

Christian P. N. Tanner − *Department of Chemistry, University of California, Berkeley, California 94720, United States*

Justin C. Ondry − *Department of Chemistry, James Franck Institute, and Pritzker School of Molecular Engineering, University of Chicago, Chicago, Illinois 60637, United States;* orcid.org/0000-0001-9113-3420

Chenkun Zhou − *Department of Chemistry, James Franck Institute, and Pritzker School of Molecular Engineering, University of Chicago, Chicago, Illinois 60637, United States;* orcid.org/0000-0001-9388-7517

Zehan Mi − *Department of Chemistry, James Franck Institute, and Pritzker School of Molecular Engineering, University of Chicago, Chicago, Illinois 60637, United States*

Youssef A. Tazoui − *Department of Chemistry, James Franck Institute, and Pritzker School of Molecular Engineering, University of Chicago, Chicago, Illinois 60637, United States*

Byeongdu Lee − *X-ray Science Division, Argonne National Laboratory, Lemont, Illinois 60439, United States;* orcid.org/0000-0003-2514-8805

Vivian R. K. Wall − *Department of Chemistry, University of California, Berkeley, California 94720, United States*

Naomi S. Ginsberg − *Department of Chemistry, University of California, Berkeley, California 94720, United States; Department of Physics and Kavli Energy NanoSciences Institute, University of California, Berkeley, California 94720, United States; Molecular Biophysics and Integrated Bioimaging Division and Materials Sciences and Chemical Sciences Divisions, Lawrence Berkeley National Laboratory, Berkeley, California 94720, United States; STROBE, NSF Science & Technology Center, Berkeley, California 94720, United States;* orcid.org/0000-0002-5660-3586

Complete contact information is available at: https://pubs.acs.org/10.1021/acsnano.4c06033

Author Contributions

○A.J. and J.P. have contributed equally.

Notes

The authors declare no competing financial interest.

Preprint: Ahhyun Jeong; Josh Portner; Christian P. N. Tanner; Justin C. Ondry; Chenkun Zhou; Zehan Mi; Youssef A. Tazoui; Vivian R. K. Wall; Naomi S. Ginsberg; and Dmitri V. Talapin. Colloidal dispersions of sterically and electrostatically stabilized PbS quantum dots: the effect of the stabilization mechanism on structure factors, second virial coefficients, and film-forming properties. 2024. arXiv:2404.18915. arXiv Preprint. URL: https://arxiv.org/abs/2404.18915 (Accessed Oct 14, 2024).

ACKNOWLEDGMENTS

We are grateful to Dr. A. Nelson for a critical reading and editing of the manuscript. We thank Dr. X. Zuo for support for X-ray scattering experiments in Advanced Photon Source, Argonne National Laboratory, and Dr. J. F. Douglas (NIST) for fruitful discussions. We are grateful to S. Kunstelj for help with FTIR measurement. We acknowledge the European XFEL in Schenefeld, Germany, for provision of X-ray free electron laser beamtime at Scientific Instrument MID (Materials Imaging and Dynamics) under proposal number 3099 and would like to thank the staff for their assistance. Material synthesis and optimizations were supported by the University of Chicago Materials Research Science and Engineering Center, supported by National Science Foundation under award number DMR-2011854. X-ray scattering, X-FEL experiments, and simulations were supported by the Office of Basic Energy Sciences (BES), US Department of Energy (DOE) (award no. DE-SC0019375). A.J. was partially supported by Kwanjeong Educational Foundation. C.P.N.T. and V.R.K.W. were supported by the NSF (Graduate Research Fellowship no. DGE1106400). Z.M. is supported by the University of Chicago MRSEC Graduate Fellowship. Y.A.T. was supported by University of Chicago's Prototype for Success Program and the Quad Undergraduate Research Scholars Program. N.S.G. was supported by a David and Lucile Packard Foundation Fellowship for Science and Engineering and Camille and a Henry Dreyfus Teacher-Scholar Award. Use of the Stanford Synchrotron Radiation Light Source, SLAC National Accelerator Laboratory, is supported by the DOE, Office of Science, Office of Basic Energy Sciences (contract no. DE-AC02-76SF00515). Work performed at the Center for Nanoscale Materials and Advanced Photon Source, U.S. Department of Energy Office of Science User Facilities, was supported by the U.S. DOE, Office of Basic Energy Sciences, under Contract no. DE-AC02-06CH11357.

REFERENCES

(1) García de Arquer, F. P.; Talapin, D. V.; Klimov, V. I.; Arakawa, Y.; Bayer, M.; Sargent, E. H. Semiconductor quantum dots: Technological progress and future challenges. *Science* **2021**, *373* (6555), 640.

(2) Liu, M. X.; Yazdani, N.; Yarema, M.; Jansen, M.; Wood, V.; Sargent, E. H. Colloidal quantum dot electronics. *Nat. Electron* **2021**, *4* (8), 548−558.

(3) Li, P.; Kim, S.; Tian, B. Beyond 25 years of biomedical innovation in nano-bioelectronics. *Device* **2024**, *2* (7), 100401.

(4) Li, P. J.; Kim, S.; Tian, B. Z. Nanoenabled Trainable Systems: From Biointerfaces to Biomimetics. *ACS Nano* **2022**, *16* (12), 19651−19664.

(5) Carey, G. H.; Abdelhady, A. L.; Ning, Z. J.; Thon, S. M.; Bakr, O. M.; Sargent, E. H. Colloidal Quantum Dot Solar Cells. *Chem. Rev.* **2015**, *115* (23), 12732−12763.

(6) Wu, Z. X.; Ou, Y. D.; Cai, M. Q.; Wang, Y. H.; Tang, R. X.; Xia, Y. Short-Wave Infrared Photodetectors and Imaging Sensors Based on Lead Chalcogenide Colloidal Quantum Dots. *Adv. Opt. Mater.* **2023**, *11* (1), 2201577.

(7) Kim, J.; Song, S.; Kim, Y. H.; Park, S. K. Recent Progress of Quantum Dot-Based Photonic Devices and Systems: A Comprehensive Review of Materials, Devices, and Applications. *Small Struct* **2021**, *2* (3), 2000024.

(8) Balazs, D. M.; Loi, M. A. Lead-Chalcogenide Colloidal-Quantum-Dot Solids: Novel Assembly Methods, Electronic Structure Control, and Application Prospects. *Adv. Mater.* **2018**, *30* (33), 1800082.

(9) Shang, Y. Q.; Ning, Z. J. Colloidal quantum-dots surface and device structure engineering for high-performance light-emitting diodes. *Natl. Sci. Rev.* **2017**, *4* (2), 170−183.

(10) Boles, M. A.; Ling, D.; Hyeon, T.; Talapin, D. V. The surface science of nanocrystals. *Nat. Mater.* **2016**, *15* (2), 141−153.

(11) Kovalenko, M. V.; Scheele, M.; Talapin, D. V. Colloidal Nanocrystals with Molecular Metal Chalcogenide Surface Ligands. *Science* **2009**, *324* (5933), 1417−1420.

(12) Kovalenko, M. V.; Bodnarchuk, M. I.; Zaumseil, J.; Lee, J. S.; Talapin, D. V. Expanding the Chemical Versatility of Colloidal Nanocrystals Capped with Molecular Metal Chalcogenide Ligands. *J. Am. Chem. Soc.* **2010**, *132* (29), 10085−10092.

(13) Dirin, D. N.; Dreyfuss, S.; Bodnarchuk, M. I.; Nedelcu, G.; Papagiorgis, P.; Itskos, G.; Kovalenko, M. V. Lead Halide Perovskites and Other Metal Halide Complexes As Inorganic Capping Ligands for Colloidal Nanocrystals. *J. Am. Chem. Soc.* **2014**, *136* (18), 6550−6553.

(14) Zhang, H.; Jang, J.; Liu, W. Y.; Talapin, D. V. Colloidal Nanocrystals with Inorganic Halide, Pseudohalide, and Halometallate Ligands. *ACS Nano* **2014**, *8* (7), 7359−7369.

(15) Liu, W. Y.; Lee, J. S.; Talapin, D. V. III-V Nanocrystals Capped with Molecular Metal Chalcogenide Ligands: High Electron Mobility and Ambipolar Photoresponse. *J. Am. Chem. Soc.* **2013**, *135* (4), 1349−1357.

(16) Bederak, D.; Balazs, D. M.; Sukharevska, N. V.; Shulga, A. G.; Abdu-Aguye, M.; Dirin, D. N.; Kovalenko, M. V.; Loi, M. A. Comparing Halide Ligands in PbS Colloidal Quantum Dots for Field-Effect Transistors and Solar Cells. *ACS Appl. Nano Mater.* **2018**, *1* (12), 6882−6889.

(17) Lee, J. S.; Kovalenko, M. V.; Huang, J.; Chung, D. S.; Talapin, D. V. Band-like transport, high electron mobility and high photoconductivity in all-inorganic nanocrystal arrays. *Nat. Nanotechnol.* **2011**, *6* (6), 348−352.

(18) Boles, M. A.; Engel, M.; Talapin, D. V. Self-Assembly of Colloidal Nanocrystals: From Intricate Structures to Functional Materials. *Chem. Rev.* **2016**, *116* (18), 11220−11289.

(19) Talapin, D. V.; Engel, M.; Braun, P. V. Functional materials and devices by self-assembly. *MRS Bull.* **2020**, *45* (10), 799−806.

(20) Zhuang, Y.; Charbonneau, P. Recent Advances in the Theory and Simulation of Model Colloidal Microphase Formers. *J. Phys. Chem. B* **2016**, *120* (32), 7775−7782.

(21) Krishnamoorthy, S.; Hinderling, C.; Heinzelmann, H. Nanoscale patterning with block copolymers. *Mater. Today* **2006**, *9* (9), 40−47.

(22) Li, M. Q.; Ober, C. K. Block copolymer patterns and templates. *Mater. Today* **2006**, *9* (9), 30−39.

(23) Doblas, D.; Kister, T.; Cano-Bonilla, M.; Gonzalez-Garcia, L.; Kraus, T. Colloidal Solubility and Agglomeration of Apolar Nanoparticles in Different Solvents. *Nano Lett.* **2019**, *19* (8), 5246−5252.

(24) Kister, T.; Monego, D.; Mulvaney, P.; Widmer-Cooper, A.; Kraus, T. Colloidal Stability of Apolar Nanoparticles: The Role of Particle Size and Ligand Shell Structure. *ACS Nano* **2018**, *12* (6), 5969−5977.

(25) Monego, D.; Kister, T.; Kirkwood, N.; Doblas, D.; Mulvaney, P.; Kraus, T.; Widmer-Cooper, A. When Like Destabilizes Like: Inverted Solvent Effects in Apolar Nanoparticle Dispersions. *ACS Nano* **2020**, *14* (5), 5278−5287.

(26) Monego, D.; Kister, T.; Kirkwood, N.; Mulvaney, P.; Widmer-Cooper, A.; Kraus, T. Colloidal Stability of Apolar Nanoparticles: Role of Ligand Length. *Langmuir* **2018**, *34* (43), 12982−12989.

(27) van Rijssel, J.; Peters, V. F. D.; Meeldijk, J. D.; Kortschot, R. J.; van Dijk-Moes, R. J. A.; Petukhov, A. V.; Erne, B. H.; Philipse, A. P. Size-Dependent Second Virial Coefficients of Quantum Dots from Quantitative Cryogenic Electron Microscopy. *J. Phys. Chem. B* **2014**, *118* (37), 11000−11005.

(28) Israelachvili, J. N. Chapter 14: Electrostatic Forces between Surfaces in Liquids. In *Intermolecular and Surface Forces*, 3 ed.; Academic Press: Burlington, MA, 2011; pp 291−340. rd ed..

(29) Derjaguin, B. A Theory of Interaction of Particles in Presence of Electric Double-Layers and the Stability of Lyophobe Colloids and Disperse Systems. *Prog. Surf. Sci.* **1993**, *43* (1−4), 1−14.

(30) Derjaguin, B.; Landau, L. Theory of the Stability of Strongly Charged Lyophobic Sols and of the Adhesion of Strongly Charged-Particles in Solutions of Electrolytes. *Prog. Surf. Sci.* **1993**, *43* (1−4), 30−59.

(31) Verwey, E. J. W. Theory of the Stability of Lyophobic Colloids. *J. Phys. Colloid Chem.* **1947**, *51* (3), 631−636.

(32) Coropceanu, I.; Janke, E. M.; Portner, J.; Haubold, D.; Nguyen, T. D.; Das, A.; Tanner, C. P. N.; Utterback, J. K.; Teitelbaum, S. W.; Hudson, M. H.; et al. Self-assembly of nanocrystals into strongly electronically coupled all-inorganic supercrystals. *Science* **2022**, *375* (6587), 1422−1426.

(33) Tanner, C. P.; Wall, V. R.; Portner, J.; Jeong, A.; Das, A.; Utterback, J. K.; Hamerlynck, L. M.; Raybin, J. G.; Hurley, M. J.; Leonard, N.; Wai, R. B.; Tan, J. A.; Gababa, M.; Zhu, C.; Schaible, E.; Tassone, C. J.; Limmer, D. T.; Teitelbaum, S. W.; Talapin, D. V.; Ginsberg, N. S. Enhancing nanocrystal superlattice self-assembly near a metastable liquid binodal. *arXiv Preprint* **2024**, arXiv:2404.16808.

(34) Tanner, C. P. N.; Utterback, J. K.; Portner, J.; Coropceanu, I.; Das, A.; Tassone, C. J.; Teitelbaum, S. W.; Limmer, D. T.; Talapin, D. V.; Ginsberg, N. S. In Situ X-ray Scattering Reveals Coarsening Rates of Superlattices Self-Assembled from Electrostatically Stabilized Metal Nanocrystals Depend Nonmonotonically on Driving Force. *ACS Nano* **2024**, *18* (7), 5778−5789.

(35) Hendricks, M. P.; Campos, M. P.; Cleveland, G. T.; Jen-La Plante, I.; Owen, J. S. A tunable library of substituted thiourea precursors to metal sulfide nanocrystals. *Science* **2015**, *348* (6240), 1226−1230.

(36) Protesescu, L.; Nachtegaal, M.; Voznyy, O.; Borovinskaya, O.; Rossini, A. J.; Emsley, L.; Copéret, C.; Günther, D.; Sargent, E. H.; Kovalenko, M. V. Atomistic Description of Thiostannate-Capped CdSe Nanocrystals: Retention of Four-Coordinate SnS4Motif and Preservation of Cd-Rich Stoichiometry. *J. Am. Chem. Soc.* **2015**, *137* (5), 1862−1874.

(37) Boles, M. A.; Talapin, D. V. Binary Assembly of PbS and Au Nanocrystals: Patchy PbS Surface Ligand Coverage Stabilizes the CuAu Superlattice. *ACS Nano* **2019**, *13* (5), 5375−5384.

(38) Li, T.; Senesi, A. J.; Lee, B. Small Angle X-ray Scattering for Nanoparticle Research. *Chem. Rev.* **2016**, *116* (18), 11128−11180.

https://doi.org/10.1021/acsnano.4c06033
ACS Nano 2024, 18, 33864−33874

(39) Sirota, E. B.; Ouyang, H. D.; Sinha, S. K.; Chaikin, P. M.; Axe, J. D.; Fujii, Y. Complete Phase-Diagram of a Charged Colloidal System - a Synchrotron X-Ray-Scattering Study. *Phys. Rev. Lett.* **1989**, *62* (13), 1524−1527.
(40) Bishop, K. J. M.; Wilmer, C. E.; Soh, S.; Grzybowski, B. A. Nanoscale Forces and Their Uses in Self-Assembly. *Small* **2009**, *5* (14), 1600−1630.
(41) Ofosu, C. K.; Kang, J. H.; Truskett, T. M.; Milliron, D. J. Effective Hard-Sphere Repulsions between Oleate-Capped Colloidal Metal Oxide Nanocrystals. *J. Phys. Chem. Lett.* **2022**, *13* (48), 11323−11329.
(42) Stradner, A.; Sedgwick, H.; Cardinaux, F.; Poon, W. C. K.; Egelhaaf, S. U.; Schurtenberger, P. Equilibrium cluster formation in concentrated protein solutions and colloids. *Nature* **2004**, *432* (7016), 492−495.
(43) Wertheim, M. S. Exact Solution of Percus-Yevick Integral Equation for Hard Spheres. *Phys. Rev. Lett.* **1963**, *10* (8), 321.
(44) Heinen, M.; Holmqvist, P.; Banchio, A. J.; Nägele, G. Erratum: "Pair structure of the hard-sphere Yukawa fluid: An improved analytic method versus simulations, Rogers-Young scheme, and experiment" [J. Chem. Phys. 134, 044532 (2011)]. *J. Chem. Phys.* **2011**, *134* (12), 129901.
(45) Biehl, R. Jscatter, a program for evaluation and analysis of experimental data. *PLoS One* **2019**, *14* (6), No. e0218789.
(46) Chremos, A.; Douglas, J. F. Hidden Hyperuniformity in Soft Polymeric Materials. *Phys. Rev. Lett.* **2018**, *121* (25), 258002.
(47) Tanner, C. P.; Wall, V. R.; Gababa, M.; Portner, J.; Jeong, A.; Hurley, M. J.; Leonard, N.; Raybin, J. G.; Utterback, J. K.; Kim, A.; Fluerasu, A.; Sun, Y.; Möller, J.; Zozulya, A.; Jo, W.; Madsen, A.; Talapin, D. V.; Teitelbaum, S. W.; Ginsberg, N. S. Suppressed self-diffusion of nanoscale constituents of a complex liquid. *arXiv Preprint* **2024**, arXiv:2404.17756.
(48) Chremos, A.; Douglas, J. F. Particle localization and hyperuniformity of polymer-grafted nanoparticle materials. *Ann. Phys-Berlin* **2017**, *529* (5), 1600342.
(49) Kohonen, M. M.; Karaman, M. E.; Pashley, R. M. Debye length in multivalent electrolyte solutions. *Langmuir* **2000**, *16* (13), 5749−5753.
(50) Chremos, A.; Douglas, J. F. Communication: Counter-ion solvation and anomalous low-angle scattering in salt-free polyelectrolyte solutions. *J. Chem. Phys.* **2017**, *147* (24), 241103.
(51) Bonneté, F.; Finet, S.; Tardieu, A. Second virial coefficient: variations with lysozyme crystallization conditions. *J. Cryst. Growth* **1999**, *196* (2−4), 403−414.
(52) Haxton, T. K.; Whitelam, S. Design rules for the self-assembly of a protein crystal. *Soft Matter* **2012**, *8* (13), 3558−3562.
(53) Tanabe, Y.; Muller, N.; Fischer, E. W. Density Fluctuation in Amorphous Polymers by Small-Angle X-Ray-Scattering. *Polym. J.* **1984**, *16* (6), 445−452.
(54) Leader, G. R.; Gormley, J. F. The Dielectric Constant of N-Methylamides. *J. Am. Chem. Soc.* **1951**, *73* (12), 5731−5733.
(55) Sengwa, R. J.; Khatri, V.; Sankhla, S. Static Dielectric Constants and Kirkwood Correlation Factor of the Binary Mixtures of N-Methylformamide with Formamide, N,N-Dimethylformamide and N,N-Dimethylacetamide. *J. Solution Chem.* **2009**, *38* (6), 763−769.
(56) Bini, M.; Brancolini, G.; Tozzini, V. Aggregation behavior of nanoparticles: Revisiting the phase diagram of colloids. *Front Mol. Biosci* **2022**, *9*, 986223.
(57) Ruiz-Franco, J.; Zaccarelli, E. On the Role of Competing Interactions in Charged Colloids with Short-Range Attraction. *Annu. Rev. Conden Ma P* **2021**, *12*, 51−70.
(58) Banchio, A. J.; Nägele, G. Short-time transport properties in dense suspensions:: From neutral to charge-stabilized colloidal spheres. *J. Chem. Phys.* **2008**, *128* (10), 104903.
(59) Ioannidou, K.; Kanduc, M.; Li, L. N.; Frenkel, D.; Dobnikar, J.; Del Gado, E. The crucial effect of early-stage gelation on the mechanical properties of cement hydrates. *Nat. Commun.* **2016**, *7*, 12106.
(60) Zhang, Z. H.; Liu, Y. Recent progresses of understanding the viscosity of concentrated protein solutions. *Curr. Opin Chem. Eng.* **2017**, *16*, 48−55.
(61) Gapinski, J.; Wilk, A.; Patkowski, A.; Häußler, W.; Banchio, A. J.; Pecora, R.; Nägele, G. Diffusion and microstructural properties of solutions of charged nanosized proteins: Experiment versus theory. *J. Chem. Phys.* **2005**, *123* (5), 054708.
(62) Saunders, A. E.; Korgel, B. A. Second virial coefficient measurements of dilute gold nanocrystal dispersions using small-angle X-ray scattering. *J. Phys. Chem. B* **2004**, *108* (43), 16732−16738.
(63) Missoni, L. L.; Tagliazucchi, M. The Phase Behavior of Nanoparticle Superlattices in the Presence of a Solvent. *ACS Nano* **2020**, *14* (5), 5649−5658.
(64) Rupich, S. M.; Shevchenko, E. V.; Bodnarchuk, M. I.; Lee, B.; Talapin, D. V. Size-Dependent Multiple Twinning in Nanocrystal Superlattices. *J. Am. Chem. Soc.* **2010**, *132* (1), 289−296.
(65) Kagan, C. R.; Murray, C. B. Charge transport in strongly coupled quantum dot solids. *Nat. Nanotechnol.* **2015**, *10* (12), 1013−1026.

https://doi.org/10.1021/acsnano.4c06033
ACS Nano 2024, 18, 33864−33874